

# Momentum-space and real-space Berry curvatures in $\text{Mn}_3\text{Sn}$

Xiaokang Li<sup>1</sup>, Liangcai Xu<sup>1</sup>, Huakun Zuo<sup>1</sup>, Alaska Subedi <sup>2,3</sup>, Zengwei Zhu<sup>1,\*</sup> and Kamran Behnia<sup>1,4,\*</sup>

(1) *Wuhan National High Magnetic Field Center*

*School of Physics, Huazhong University of Science and Technology,  
Wuhan 430074, China*

(2) *Centre de Physique Théorique,*

*École Polytechnique, CNRS, Université Paris-Saclay,  
Route de Saclay, 91128 Palaiseau, France*

(3) *Collège de France,*

*11 place Marcelin Berthelot, 75005 Paris, France*

(4) *Laboratoire de Physique Et Etude des Matériaux (UPMC-CNRS),  
ESPCI Paris, PSL Research University  
75005 Paris, France*

(Dated: February 1, 2018)

Non-collinear antiferromagnets can host a large anomalous Hall effect (AHE), as demonstrated in the case of  $\text{Mn}_3\text{X}$  ( $\text{X} = \text{Sn}, \text{Ge}$ ). Weyl nodes in the electronic dispersions are believed to cause this AHE. Their locus in the momentum space is yet to be pinned down. Here we show that in  $\text{Mn}_3\text{Sn}$  crystals in the presence of a moderate magnetic field, spin texture sets the orientation of the  $k$ -space Berry curvature, and the in-plane anisotropy due to the hexagonal Brillouin zone and Fermi surface is vanishingly small. The measured threshold magnetic field for domain nucleation points to a remarkably large energy cost for building domain walls. In the multidomain regime restricted to a narrow field window, these walls generate real-space Berry curvature, pointing to a non-trivial texture with a non-coplanar component and reminiscent of the skyrmion lattice in  $\text{MnSi}$ . In contrast to the latter case, the real-space component constitutes a sizeable fraction of the total anomalous Hall conductivity.

The  $\text{Mn}_3\text{X}$  ( $\text{X} = \text{Sn}, \text{Ge}$ ) family of compounds crystallizing in the  $\text{DO}_{19}$  HCP Bravais lattice are triangular antiferromagnets with a Néel temperature around 400 K [1, 2]. The recent observation of the anomalous Hall effect (AHE) in these systems [4, 5] followed theoretical predictions [6, 7] of nonvanishing Berry curvature in a noncollinear yet planar antiferromagnet. The discovery was followed by the detection of anomalous Nernst[8, 9] and anomalous Righi-Leduc[9] effects, the thermoelectric and thermal counterparts of the AHE, respectively. The latter observations confirmed that the zero-field transverse anomalous currents are due to the Fermi-surface quasiparticles, as argued by Haldane [10]. Several *ab initio* calculations [8, 11] have found an anomalous Hall conductivity (AHC) matching what experiments find at low temperatures. The precise configuration of spins and the locus of the Weyl nodes in the  $k$ -space generating the Berry curvature that cause these phenomena are still subject to debate.

The Hall resistivity of  $\text{Mn}_3\text{Sn}$  has a peculiar profile (see Fig. 1). Recognizably different from the AHE signal resolved in ordinary ferromagnets like bcc iron [9, 12, 13] or cobalt [14], it is also quite distinct from the much-studied spiral helimagnet  $\text{MnSi}$  [7, 8]. In contrast to these cases, in  $\text{Mn}_3\text{Sn}$ ,  $\rho_{ij}$  presents a hysteretic jump dwarfing the slope caused by the ordinary Hall conductivity. The hysteresis has a shape unlike the sigmoid commonly seen in ferromagnets [17]. Finally, the asymmetry of this loop contrasts with the symmetric hysteresis of the quantum AHE observed in magnetic two-dimensional topological insulators [18, 19].

In this paper, we show that the peculiarity of this hysteresis loop resides in the existence of a threshold field  $B_0$  for domain nucleation. Three distinct regimes can be identified. In regime I, below  $B_0$ , there is a single magnetic domain with an orientation set by the sample history and not by the applied field. In regime II, above  $B_0$ , multiple domains coexist, and, as the magnetic field increases, the domain favored by it occupies a larger portion of the sample. At sufficiently higher fields (regime III), the sample becomes single domain again, and the domain orientation is now entirely set by the magnetic field. Monitoring the electric field generated by a rotating in-plane magnetic field in regime III, we find that the finite component of the AHC tensor is set by the orientation of spins and not by the underlying lattice. This observation is backed by theoretical calculations, which find that the single-ion anisotropy is vanishingly small and the Fermi surface is not modified by rotation of spins. It also has implications for the ongoing effort to pin down the source of the Berry curvature in the reciprocal space. The magnitudes of  $B_0$  and the jump in magnetization can be used to quantify the energy cost of erecting domain walls. Finally, we find that  $\rho_{ij}^A$  ceases to be proportional to magnetization in the boundary between regimes II and III. Such a ‘topological Hall effect’ (THE) has been commonly attributed to the accumulation of the Berry curvature in the real space [20] due to the consequence of a non-trivial magnetic texture, such as a skyrmion lattice in the phase A of  $\text{MnSi}$ [7]. Thus, when  $\text{Mn}_3\text{Sn}$  is single domain, the AHE is uniquely caused by momentum-space Berry curvature. But when it is multi-

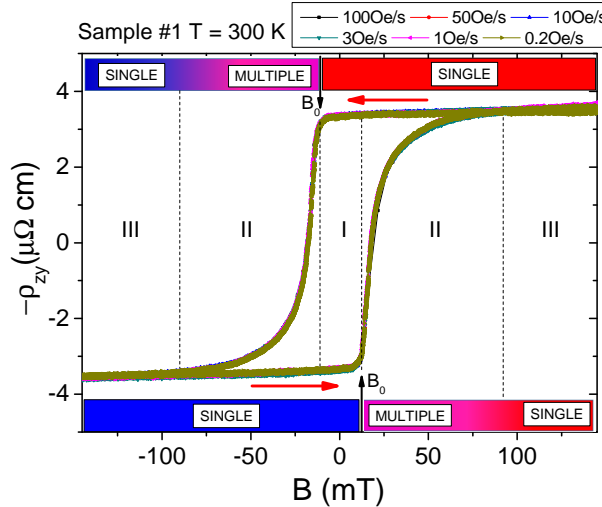


**FIG. 1. Hysteretic anomalous Hall effect in  $\text{Mn}_3\text{Sn}$ :**  $\rho_{yz}^A$  as a function of magnetic field in  $\text{Mn}_3\text{Sn}$  has a peculiar shape. Three different regimes can be identified. When the field is lower than  $B_0$ , marked by a vertical arrow, the spins keep their configuration regardless of the magnetic field (regime I). When  $B > B_0$  (regime II), new magnetic domains are induced by the magnetic field. At sufficiently high fields, the sample becomes single-domain again (regime III). The hysteretic loop is reproducible even when the sweeping rate changes by a factor of five hundred.

domain, domain walls generate a real-space Berry curvature and an additional contribution to the AHE. This implies a noncoplanar spin component for domain walls.

Fig. 1 shows the hysteretic loop of  $\rho_{ij}(B)$  at the room temperature in a millimetric  $\text{Mn}_3\text{Sn}$  single crystal. When the magnetic field attains a magnitude as low as 0.2 T,  $\rho_{ij}$  locks into a finite magnitude and does not show any further evolution besides the tiny slope due to the ordinary Hall effect. When the field is swept back to zero,  $\rho_{ij}(B)$  remains locked to its magnitude. Only when the field, oriented along the opposite direction, attains a specific amplitude, which we call  $B_0$ ,  $\rho_{ij}(B)$  begins to change steeply. Upon further increase,  $\rho_{ij}(B)$  saturates to a value opposite in sign but identical in magnitude to its initial value. As seen in the figure, repeating this procedure numerous times with different sweeping rates reproduces the same curve. This is very different from the hysteretic magnetization profile seen in ferromagnets, which has a “sigmoid” shape [17], but is remarkably similar to the hysteretic loop of magnetization resolved in a ferromagnetic liquid crystal [21]. In the former case, the shape of the hysteretic loop is set by the displacement of domain walls and their pinning by defects. The loop is smooth, and the passage between single-domain and multidomain regimes in its two ends are symmetric[17].

The existence of a finite threshold field for domain nucleation implies that, below this field, tolerating a magnetization opposite to the applied field is not as costly in energy than erecting a domain wall. At  $B_0$ , the two

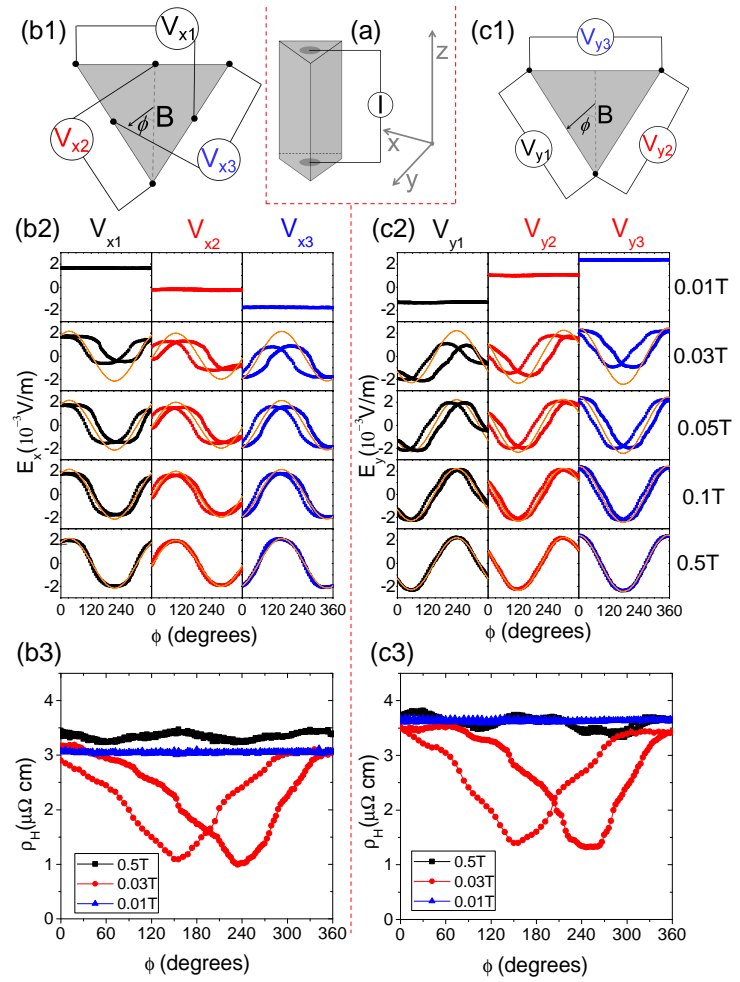


**FIG. 2. Angle-dependent Hall resistivity:** a) The current was applied along the  $z$ -axis of a sample with a triangular cross section and the magnetic field was rotated in the basal plane. Each pair of electrodes monitored the electric field along one of the three equivalent  $x$ -axes (b1) or the three  $y$ -axes (c1). Angular variation of the three  $E_x$  and the three  $E_y$  as a function of the angle between magnetic field and the  $x$ -axis are shown in (b2) and (c2). At low magnetic field (regime I), the total electric field remains unchanged. At high magnetic field (regime III), the measured electric field becomes sinusoidal (shown as a red line). In the intermediate field range (regime II), the electric field is non-sinusoidal and strongly hysteretic. Panels (b3) and (c3) show  $\rho_H = |E|/J$ , where  $|E|$  represents the magnitude of the total electric field vector extracted from its projections. It is almost the same in regimes I and III. The fluctuations in regime III set an upper bound to any in-plane anisotropy undetectable by this experiment.

costs become equal and domain reversal starts. Insensitivity to the sweep rate suggests thermodynamic equilibrium during the entire loop. The boundary between regime I (single-domain) and regime II (multi-domain) is sharp, but the boundary between regime II and regime III (field-induced single domain) is fuzzy and, as we will see

below, hosts a specific component in  $\rho_{ij}(B)$  generated by inhomogeneous magnetization. In regime III, the signal smoothly saturates to its initial magnitude with an opposite sign, indicating an inverted single-domain regime.

Our angle-dependent study illustrates the difference between the three regimes. In this experiment, electric current was applied along the z-axis and the magnetic field rotated in the xy plane. The electric field along different orientations was monitored using multiple electrodes. In this way, we could determine the amplitude and the orientation of the total electric-field vector for an arbitrary orientation of magnetic field. We studied both a square sample [22] and a triangular sample (see Fig. 2), whose shape excluded demagnetization artifacts. The results were similar. In regime I, that is below  $B_0$ , the electric field was unaffected by rotation. In regime II, strong hysteresis was observed in the angular dependence of the signal. In regime III, each projection of the electric field along the three x- and three y-axes was found to display almost perfect sinusoids. Thus, in this regime, the spin texture is easily rotated with magnetic field. As seen in the bottom panels of Fig. 2, in both regime I and regime III, this is when the system is single-domain, the amplitude of the electric field is the same irrespective of orientation.

The first outcome of this observation is that the single-ion anisotropy is very weak. A field as small as 0.5 T easily sets the orientation of the spins by coupling to the in-plane magnetization, which is  $1.5 \times 10^{-2} \mu_B/\text{f.u.}$  at 0.5 T [5]. This corresponds to an energy as small as 0.5  $\mu\text{eV}/\text{f.u.}$ , implying a negligible single-ion anisotropy compared to the Heisenberg and Dzyaloshinskii-Moriya terms [23]. Our DFT calculations with SOC find a vanishingly small in-plane single-ion anisotropy [22], with the rigid rotation of spins by a uniform angle varying the total energy by less than 0.045 meV/Mn. In agreement with previous experimental and theoretical studies [2, 5, 24], we find a noncollinear 120-degree antiferromagnetic order with a small in-plane ferromagnetic canted moment of  $\sim 0.5 \times 10^{-2} \mu_B/\text{f.u.}$  Since neither the calculated total energy nor the canted component change upon a uniform rotation of the spins, the  $U(1)$  symmetry is not broken to a  $\mathbb{Z}_6$  anisotropy.

A second consequence is about the in-plane anisotropy of the momentum-space Berry curvature. Previous studies [4, 5, 9] detected a finite AHC for two perpendicular orientations of magnetic field. The magnitude of  $\sigma_{yz}^A(B \parallel x)$  and  $\sigma_{xz}^A(B \parallel y)$  was found to be close to each other in both Mn<sub>3</sub>Ge [5] and in Mn<sub>3</sub>Sn [9]. Measuring numerous samples [22], we also found that the anisotropy is small and below 15 percent (See Fig. 3a). Our angle-dependent experiment puts an even smaller upper bound ( $\sim 0.05$ ) on any in-plane anisotropy. Moreover, for any arbitrary orientation of magnetic field,  $\sigma_{ij}^A$  is almost the same. This is also in agreement with our DFT calculations, which find a band structure [22] and a Fermi surface unchanged as the spins rotate (Fig. 3b-e).

A finite  $\sigma_{ij}^A$  arises when  $\Omega^k$  summed over the Brillouin

zone does not vanish:

$$\sigma_{ij}^A = \frac{-e^2}{\hbar} \sum_n \int_{BZ} \frac{d^3k}{(2\pi)^3} f_n(k) \Omega_n^k(k) \quad (1)$$

The indexes  $i$ ,  $j$  and  $k$  refer to the three perpendicular orientations, which are often assimilated to the  $x$ -,  $y$ - and  $z$ -axes of the crystal lattice. Theoretical calculations [8, 11, 26-28] find Weyl nodes of opposite chirality in the vicinity of the  $k$ -points of the Brillouin zone of Mn<sub>3</sub>X materials. However, they start from different magnetic structures and do not find the nodes at the same  $k$ -space position. Because of the symmetry considerations, a finite  $\sigma_{ij}^A$  is expected along one orientation and not the other. Our result implies that the orientation along which  $\sigma_{ij}^A$  remain finite is not a crystal axis. The magnitude of AHC does not depend on the angle between the spin lattice and the underlying crystal. Given the geometry of the Fermi surface in the hexagonal plane (see Fig. 3b,c), this may be accounted for by assuming that the  $k$ -space Berry curvature reside at the  $k$ -point vertices of the hexagon hosting a small circular Fermi surface. A recent suggestion for the locus of the Weyl nodes [28] puts them close to  $k$ -points.

We now turn our attention to domain nucleation at the onset of regime II. The hysteresis loop of magnetization and Hall resistivity are shown in Fig. 4a,b. A threshold field  $B_0$  of almost identical magnitude can be identified in both. Above this field, domains with a magnetization corresponding to the orientation of the applied field nucleate in the single-domain matrix that occupies the whole sample below  $B_0$ . As the field is swept further, the minority domain grows in size and ends up entirely replacing the former majority domain. The smooth and reproducible functional form is reminiscent of the Langevin function. However, the AHE signal increases faster than the magnetization (Fig. 4c).

The hysteresis loops were followed down to 50K, below which the magnetic order is replaced with a spin-glass order [5]. In the whole temperature window, one could detect a finite  $B_0$ . Multiplying it by the jump in magnetization  $\Delta M$ , one quantifies the energy cost per volume of keeping the sample single domain. The temperature dependence of  $E_v = B_0 \Delta M$  is shown in Fig. 4d. According to the classical theory of nucleation, the first droplet of minority domains emerges when the volume energy saved by the emergence of this domain compensates the energy cost of building a domain wall  $E_S$ , which is unknown. Assuming  $E_S \sim \langle J \rangle / t^2$  where  $\langle J \rangle$  is the average interaction between neighboring spins and  $t$  the thickness of the domain wall, one can find a typical thickness of  $t = (\frac{\langle J \rangle}{B_0 \Delta M})^{1/3}$ . Taking  $\langle J \rangle \sim 5\text{meV}$ , the order of magnitude of the Heisenberg coupling between spins [23] this yields  $t \geq 100 \text{ nm}$  at room temperature in agreement with what was suggested by Liu and Balents [23] based on the stationary solution of a sine-Gordon equation.

In regime II, where the system is multi-domain, such thick domain walls can be a source of Berry curvature in

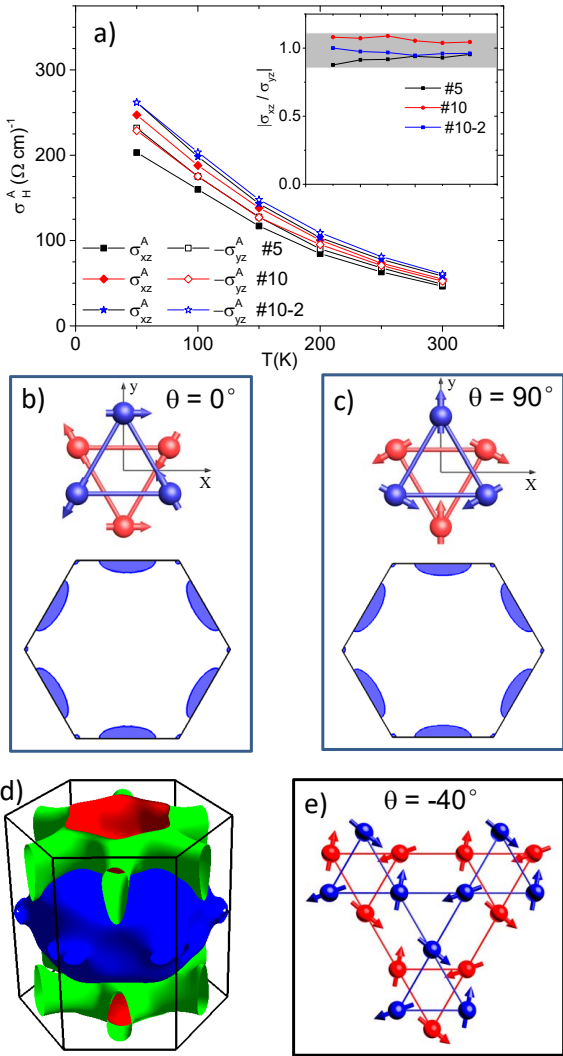


**FIG. 3. In-plane isotropy:** a) Temperature-dependence of the anomalous Hall conductivity for two perpendicular orientations of the magnetic field in three different samples. The inset shows the in-plane anisotropy found in these fixed-angle measurements and the experimental margin (in gray). c,d) Mn spins in two adjacent planes (in blue and red) together with the calculated Fermi surface for each spin configuration projected in the hexagonal  $(k_x, k_y, 0)$  plane of the Brillouin zone. The Fermi surface does not visibly change with spin rotation. Note also the small circular fermi surface at the vertices. e) The entire calculated Fermi surface of  $\text{Mn}_3\text{Sn}$  for  $\theta=0$ . Different colors show different Fermi surface sheets. e) Mn spins oriented along an arbitrary orientation in three adjacent six-spin David stars, each operating as a magnetic octupole [25].

real space distinct from the one provided in the momentum space by the Weyl nodes. Such a distinction between components of AHE was first demonstrated in the case of MnSi. Below its Curie temperature, this helimagnet hosts a large AHE, which is almost proportional to its magnetization across a wide temperature range [8], and

is caused almost totally by momentum-space Berry curvature. In its A phase and in the presence of a skyrmion lattice, an additional component to the AHE has been resolved [7] and attributed to real-space Berry curvature, which represents an effective magnetic field caused by the spatial variation of the magnetization [20, 29, 30]. In MnSi, this specific component of the AHE caused by the momentum-space Berry curvature[7] is an order of magnitude smaller than the total anomalous signal.

By comparing the field dependence of  $\rho_{ij}^A(B)$  and  $M(B)$ , we can extract a ‘topological Hall effect’ inside a hysteresis loop as reported in other systems [31, 32]. The component of the AHE which does not track the magnitude of bulk magnetization is extracted using  $\rho^{THE}(B) = \rho_{ij}^A(B) - C(M(B) - B\chi)$ , where  $\chi$  is the high-field susceptibility (the slope of the magnetization outside the hysteresis loop) and  $C$  is a constant. As one can see in Fig. 4,  $\rho^{THE}$  is finite in a narrow field window in regime II. Thick domain walls, where local magnetization smoothly changes, are a potential source of the real-space Berry curvature [20]. Note that a finite THE is expected to arise if  $\vec{n} \cdot (\frac{\partial \vec{n}}{\partial x} \times \frac{\partial \vec{n}}{\partial y})$  [33] (where  $\vec{n} = \vec{M}/M$ ), which is assimilated to the skyrmion density[7], is finite . This can only be finite if domain walls have a non-coplanar component to their magnetization. We note that here the component of AHE caused by real-space Berry curvature is a sizeable fraction of the total signal, which is in sharp contrast with the case of MnSi [7].

If the magnetization were restricted to the planes,  $\vec{n} \cdot (\frac{\partial \vec{n}}{\partial x} \times \frac{\partial \vec{n}}{\partial y})$  would point out-of-plane. Thus the final dot product would give no skyrmion number. Therefore, one is brought to assume a non-coplanar component to the magnetization of the domain walls. This conjecture is backed by another observation. Assuming a co-planar structure, the spin configuration of a wall between two domains of opposite chirality cannot keep the inversion symmetry preserved in each domain (See Fig. 5a). Now, skyrmions are expected to arise in the presence of the Dzyaloshinskii-Moriya interaction and the absence of the inversion center [34], which impedes the cancellation of the chirality induced by opposite neighbors.

Another evidence for nontrivial domain walls is the correlation found between the width of the hysteresis loop and sample dimensions. As seen in Fig. 5b, reducing the size of a single crystal does not modify the magnitude of the AHE or  $B_0$ . On the other hand, it does affect the range of regime II in a remarkably intriguing way. In this regime, the field-induced minority domain ends up eliminating the initial majority domain with a given rate  $B_s$ [22]. According to the experiment, the  $B_s$  anisotropy is equal to the anisotropy of the sample dimensions parallel and perpendicular to the magnetic field (See Fig. 5c). In other words, the boundary between minority and majority domains evolves faster with increasing magnetic field along its orientation. Exploring the origin of this phenomenon and its possible connection with a bulk-edge dichotomy would be a subject matter for both theory

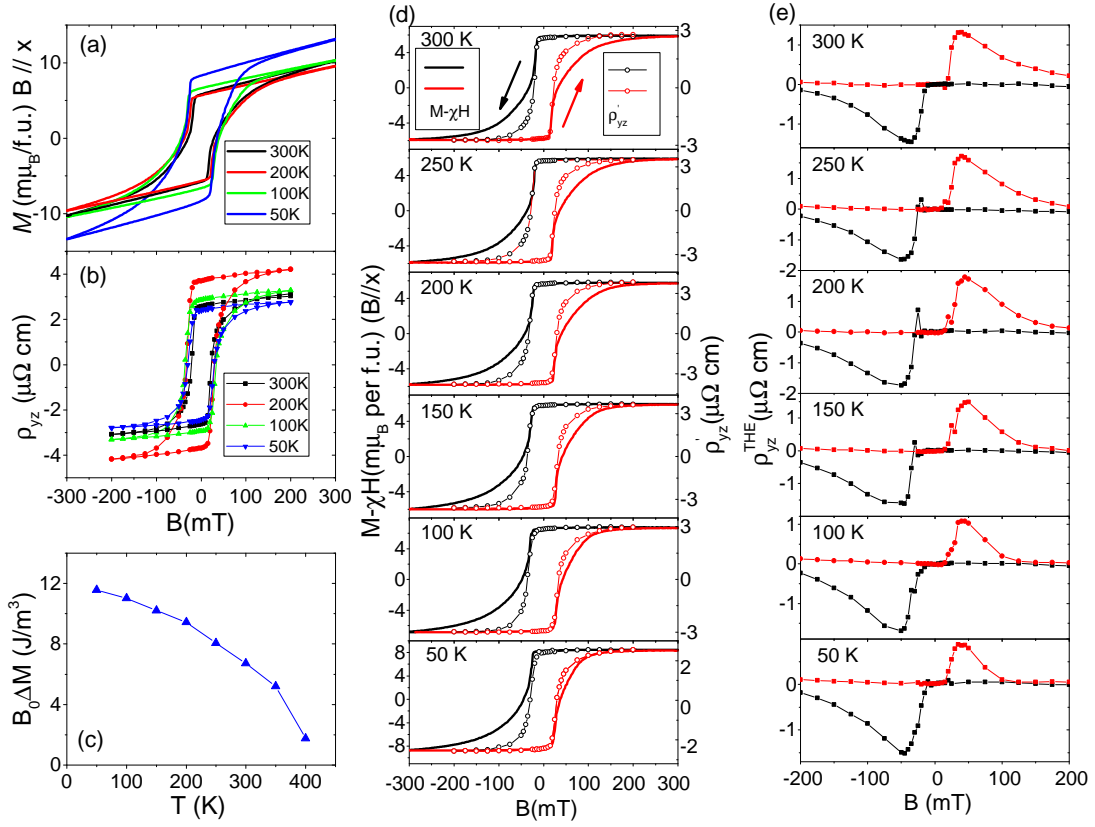


FIG. 4. **Magnetization, AHE and THE:** a) Hysteretic loops of magnetization at different temperatures. b) Hysteretic loops of  $\rho_{yz}$  at different temperatures. c) Temperature dependence of  $B_0\Delta M$ , which represents the energy cost of staying single domain. d) Comparison of the magnetization, with its high-field slope subtracted and anomalous Hall resistivity. The threshold field  $B_0$  is identical, but at all temperatures, the magnetization shows a slower variation towards saturation at the end of the hysteresis loop. e) ‘Topological Hall Effect’ resolved by subtracting normalized magnetization times a constant from the Hall resistivity at different temperatures. At the boundary of regimes II and III, a sizeable component of the AHE is due to inhomogeneous magnetization, with an out-of-plane component.

and experimental magnetic imaging.

In conclusion, let us summarize the picture of AHE in a noncollinear antiferromagnet coming out of this study. When the system is single domain and magnetization homogeneous, momentum-space Berry curvature caused by Weyl nodes is responsible for the entire AHE signal, which carries little or no signatures of the hexagonal symmetry of the lattice. In a narrow field window, there are multiple magnetic domains and an additional component to the AHE due to the real-space Berry curvature. The domain walls have a nontrivial texture and most probably a non-coplanar component. Their field-induced evolution has an intriguing correlation with the size ratio of the sample.

We acknowledge useful discussions with Leon Balents, Albert Fert, Jianpeng Liu, Achim Rosch and Binghai Yang. Z. Z. was supported by the 1000 Youth Talents Plan and the work was supported by the National Science Foundation of China (Grant No. 11574097) and The National Key Research and Development Program of China(Grant No.2016YFA0401704). K. B. was supported by China High-end foreign expert programme and Fonds-ESPCI-Paris. Computational resources were supported by the European Research Council grant ERC-319286 QMAC and the Swiss National Supercomputing Center (CSCS) under project s575.

\* [zengwei.zhu@hust.edu.cn](mailto:zengwei.zhu@hust.edu.cn)

\* [kamran.behnia@espci.fr](mailto:kamran.behnia@espci.fr)

[1] G. J. Zimmer and E. Krén, AIP Conf. Proceed. **5**, 513 (1972).

[2] S. Tomiyoshi, and Y. Yamaguchi, J. Phys. Soc. Jpn. **51**, 2478 (1982).

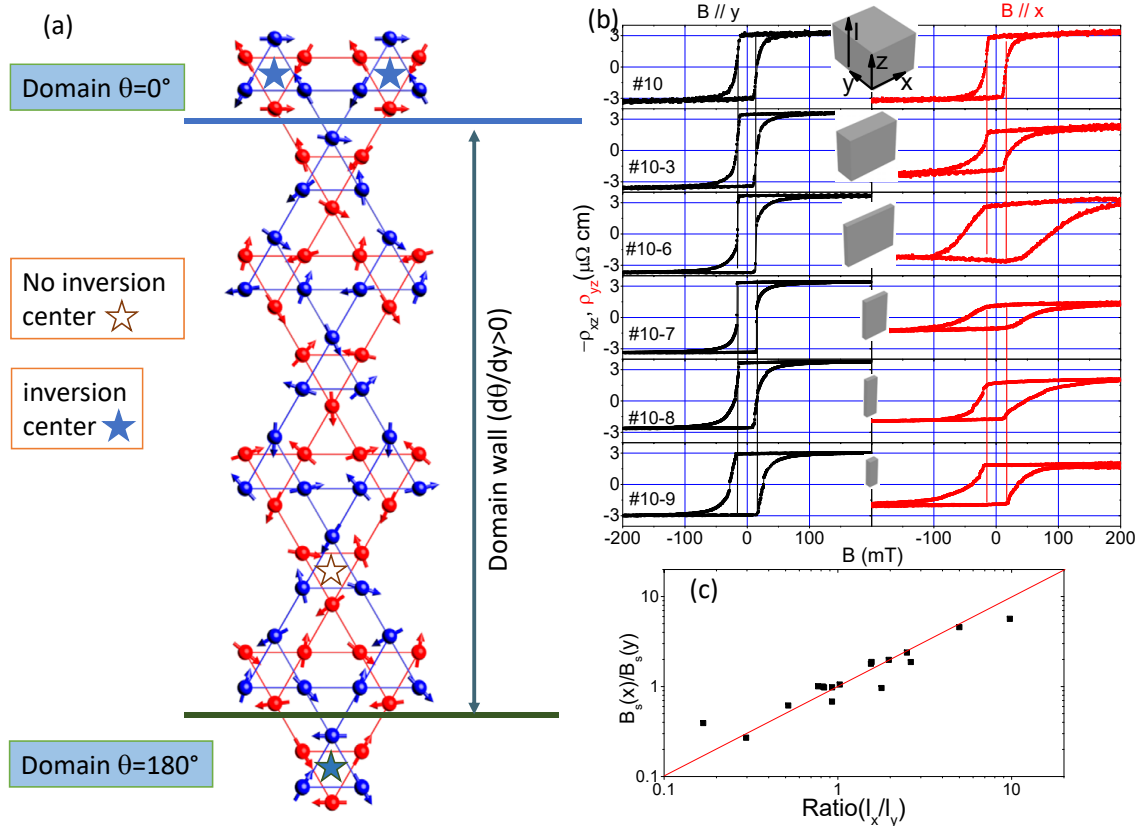


**FIG. 5. Domain walls and size dependence:** a) A domain wall between two domains of opposite chirality. Whilst in each domain, the inversion symmetry is kept, across the domain wall, it is lost due to the continuous variation of the local spin angle. This loss of inversion center provides an opportunity for the Dzyaloshinskii-Moriya interaction to generate an out-of-plane spin component, which is not shown in the present image. b) Anomalous Hall resistivity along two perpendicular orientations in a  $\text{Mn}_3\text{Sn}$  single crystal after successive reductions in the sample dimensions. Note the constancy of  $B_0$  and the variation of the loop width. c) The anisotropy of  $B_s$ , a field scale quantifying this width[22] as a function of the sample dimension ratio in a number of samples. The solid line represents  $y=x$ .

- [3] S. Nakatsuji, N. Kiyohara, and T. Higo. *Nature* **527**, 212 (2015).
- [4] A. K. Nayak *et al.* *Sci. Adv.* **2**: e1501870 (2016).
- [5] N. Kiyohara, T. Tomita, and S. Nakatsuji, *Phys. Rev. Appl.* **5**, 064009 (2016).
- [6] H. Chen, Q. Niu, and A. MacDonald, *Phys. Rev. Lett.* **112**, 017205 (2014).
- [7] J. Kübler and C. Felser, *Europhys. Lett.* **108**, 67001 (2014).
- [8] M. Ikhlas, *et al.*, *Nat. Phys.* **13**, 1085 (2017)
- [9] X. Li, *et al.*, *Phys. Rev. Lett.* **119**, 056601 (2017).
- [10] F. D. M. Haldane, *Phys. Rev. Lett.* **93**, 206602 (2004).
- [11] Y. Zhang *et al.*, *Phys. Rev. B* **95**, 075128 (2017).
- [12] P. N. Dheer, *Phys. Rev.* **156**, 637 (1967).
- [13] S. J. Watzman *et al.*, *Phys. Rev. B* **94**, 144407 (2016).
- [14] J. Kötzler and W. Gil, *Phys. Rev. B* **72**, 060412(R) (2005).
- [15] A. Neubauer, *et al.*, *Phys. Rev. Lett.* **102**, 186602 (2009).
- [16] M. Lee, Y. Onose, Y. Tokura and N. P. Ong, *Phys. Rev. B* **75**, 172403 (2007).
- [17] D.C. Jiles and D.L. Atherton, *J. Magn. Magn. Mater.* **61**, 48 (1986).
- [18] C.Z. Chang *et al.*, *Science* **340**, 167 (2013).
- [19] J. G. Checkelsky, *et al.*, *Nat. Phys.* **10**, 731 (2014).
- [20] K. Everschor-Sitte and M. Sitte, *J. Appl. Phys.* **115**, 172602 (2014).
- [21] A. Mertelj, D. Lisjak, M. Drofenik and M. Čopić, *Nature* **504**, 237 (2013).
- [22] The supplementary information can be found online.
- [23] J. Liu and L. Balent, *Phys. Rev. Lett.* **119**, 087202 (2017).
- [24] D. Zhang, *et al.*, *J. Phys.: Condens. Matter* **25** 206006 (2013).
- [25] M.-T. Suzuki, T. Koretsune, M. Ochi and R. Arita, *Phys. Rev. B* **95**, 094406 (2017)
- [26] H. Yang *et al.*, *New J. Phys.* **19** 015008(2017).
- [27] J. Kübler and C. Felser, arXiv:1711.03891 (2017).
- [28] K. Kuroda, *et al.*, *Nat. Mater.* (2017).
- [29] N. Nagaosa, X. Z. Yu, and Y. Tokura, *Philos. Trans. R. Soc., A* **370**, 5806 (2012).
- [30] F. Freimuth, R. Bamlar, Y. Mokrousov, and A. Rosch, *Phys. Rev. B* **88**, 214409 (2013).
- [31] C. Liu, *et al.*, *Phys. Rev. Lett.* **119**, 176809 (2017).
- [32] A. Soumyanarayanan *et al.*, *Nat. Mater.* **16**, 898 (2017).
- [33] P. Bruno, V. K. Dugaev, and M. Taillefumier, *Phys. Rev. Lett.* **93**, 096806 (2004).
- [34] N. Nagaosa and Y. Tokura, *Nat. Nano.* **8**, 899 (2013)

## I. THE GROWTH AND CHARACTERIZATION OF SAMPLES

$\text{Mn}_3\text{Sn}$  single crystals were grown by the vertical Bridgman technique. For the polycrystalline samples growth, the raw materials (99.999% Mn, 99.999% Sn) were weighed and mixed inside an Ar globe box with the molar ratio of 3.3:1, and then it was put in an alumina crucible which was sealed in a quartz ampule. The growth temperature was controlled at the bottom of the ampule. The material was heated up to 1100°C, remained there for 2 hour to ensure homogeneity of the melt, and was cooled down slowly to 900°C. The sample was annealed at 850°C for 20 hours and then quenched to room temperature. For the single crystal samples growth, the polycrystalline ingot was ground and put in an alumina crucible which was sealed in a quartz tube, then was hung in a vertical Bridgman furnace. In order to get better single crystal, the single crystal sample growth was repeated three times with different rates of growth. The first growth rate is 2mm/h and the last two growth rate is 1mm/h. The growth temperature is 1050°C and the growth length is 80mm. Both the poly-crystalline and single-crystalline samples were pulverized to powder for XRD measurement which confirmed the structure of  $\text{Mn}_3\text{Sn}$ . The single crystals were then cut into desired dimensions by a wire saw. The dimensions of some measured samples have been listed in the following tables.

## II. COMPUTATIONAL DETAILS

Electronic structure calculations were performed within the generalized gradient approximation (GGA) of Perdew, Burke and Ernzerhof [1] using the general full-potential linearized augmented planewave method as implemented in the ELK software package [2]. Muffin-tin radii of 2.4 and 2.6 a.u. were used for Mn and Ir, respectively. The spin-orbit coupling was treated using a second-variational scheme. A  $14 \times 14 \times 14$   $k$ -point grid was used to perform the Brillouin zone integration, and the planewave cutoff was set by  $RK_{\max} = 8$ , where  $K_{\max}$  is the planewave cutoff and  $R$  is the smallest muffin-tin radius used in the calculations (i.e. 2.4 a.u.). The energy convergence criterion was set to 0.045 meV/Mn. Experimental lattice parameters  $a = 5.665$  and  $c = 4.531$  Å and the Mn positional parameter  $x = 0.8388$  were used in all our calculations [3, 4].

## III. THE TEMPERATURE-DEPENDENCE OF MAGNETIZATION AND HALL RESISTIVITY

We measured the temperature-dependence of magnetization and Hall resistivity using a Quantum Design PPMS and VSM. In the main text, we just showed the magnetization data as the field is along  $x$  axis for a selected set of temperatures. Fig. S1 shows the complete

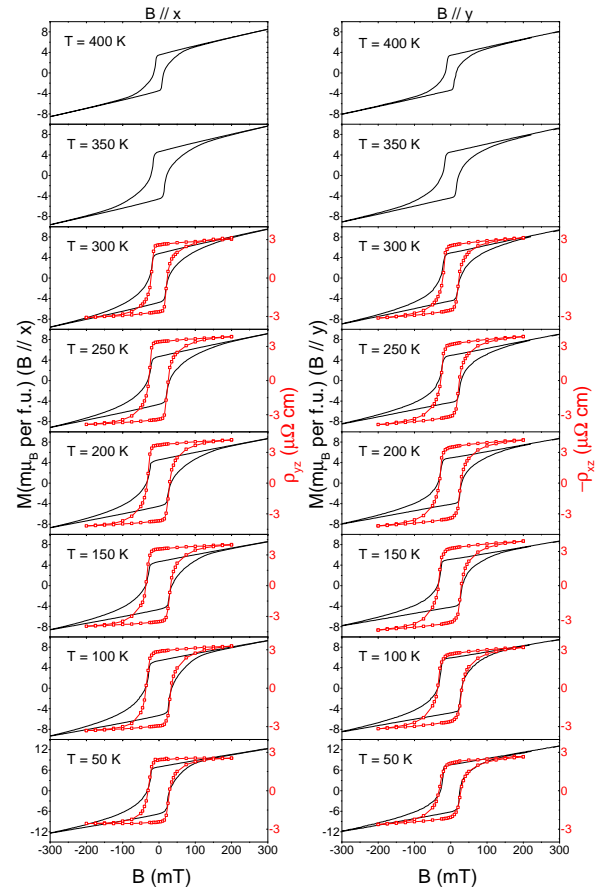


Figure S 1. The magnetization and Hall resistivity as the magnetic field along  $x$  (left column) along  $y$  (right column) at different temperatures.

set of data along both  $x$  and  $y$  axes at different temperatures. In all cases, we can extract the “Topological Hall Effect” (THE) also for a field along  $y$ -axis in the Fig. S2. The results for the two orientations are similar. We also measured the magnetization for a field along  $z$  at 300 K, shown in Fig. S3. Our data are similar to the previous report[5]. Fig. S3 shows the Hall resistivity and magnetization for three axis at 300 K, in which the magnetization data are similar to ref. S5.

## IV. MEASURING ANGLE-DEPENDENCE OF HALL RESISTIVITY IN A SAMPLE WITH A SQUARE CROSS-SECTION

We also measured the angle-dependent Hall resistivity in a sample with a square cross section in addition to the sample with a triangular cross-section discussed in the main text. As shown in Fig. S4, two pairs of electrodes perpendicular to each other monitored the electric field along the  $x$  ( $E_x$ ) and  $y$  axes ( $E_y$ ). The magnetic field was rotated in the basal plane while the current was applied along its  $z$  axis. The total Hall resistance can be de-

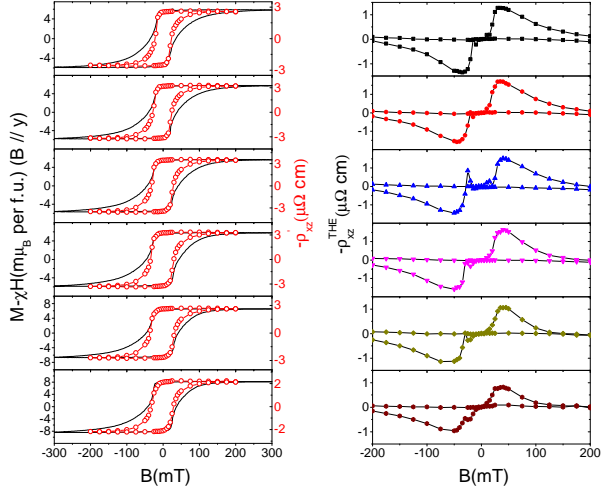


Figure S 2. a) Comparison of the magnetization, with its high-field slope subtracted and anomalous Hall resistivity as the magnetic field is along the  $y$  axis. Similar to the case of a field along the  $x$  axis showed in the main text. The threshold field  $B_0$  is identical, but the magnetization shows a slower variation at the end of the hysteresis loop. b) The topological Hall effect resolved by subtracting normalized magnetization times a constant from the Hall resistivity at different temperatures for a field along  $y$  axis.

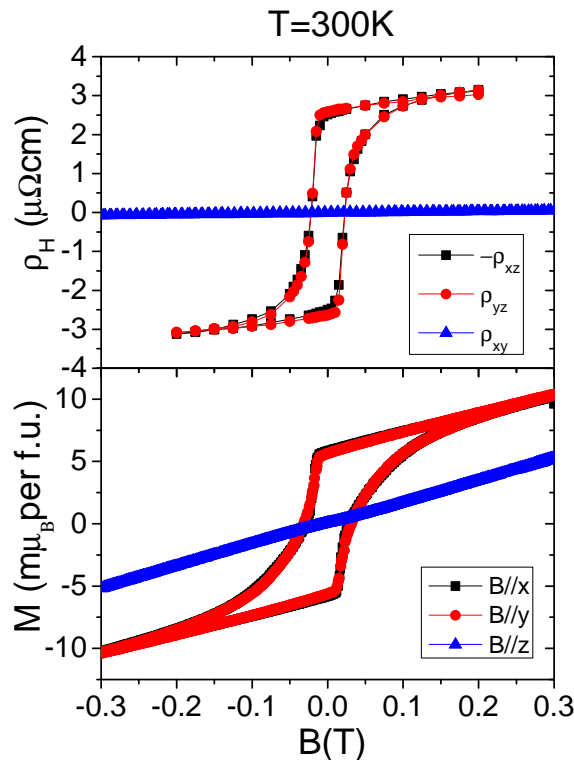


Figure S 3. The magnetization and Hall resistivity for three high-symmetric axis at 300 K.

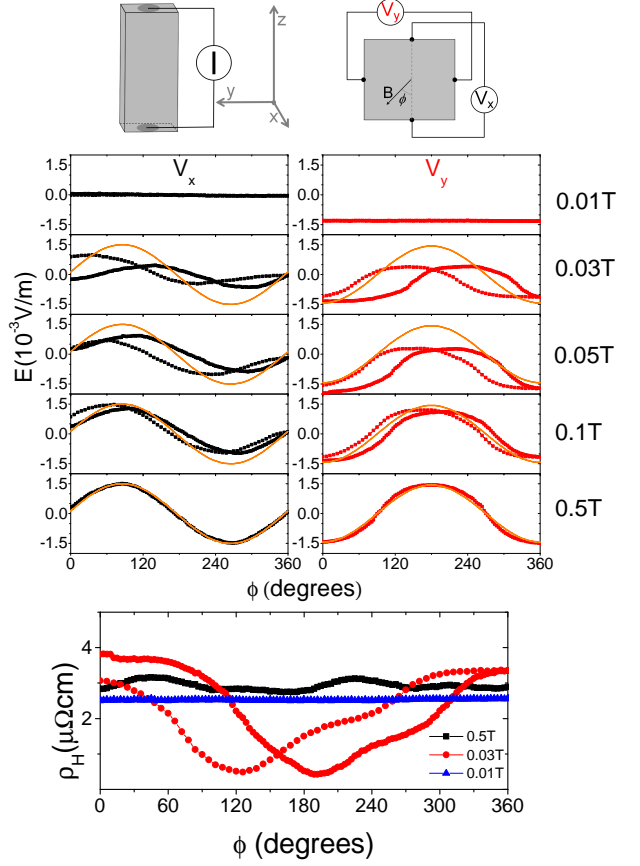


Figure S 4. a) and b) Set-up for measuring angle-dependent Hall resistivity in a sample with a quadrat cross-section. The current was applied along the  $z$  axis and the magnetic field was rotated in the basal plane. Two pairs of electrodes monitored the electric field along the  $x$  and  $y$  axes. c) Angular variation of the  $E_x$  and d) the  $E_y$  as a function of the angle between the magnetic field and the  $x$  axis. At low magnetic field (regime I), the total electric field remains unchanged. At high magnetic field (regime III), for both orientations, the measured electric field presents almost sinusoidal variation with almost no hysteresis. In the intermediate field range (regime II), the angular variation is strongly hysteretic. (e) The total Hall resistivity as a function the angle.

duced from the two electric fields:  $\rho_H = \sqrt{E_x^2 + E_y^2}/J_z$ . The results were similar to the case of a sample with a triangle cross section. The three regimes can be clearly distinguished. In regime I, with a field lower than  $B_0$ , the rotation of the magnetic field does not affect the electric field: the sample remains single domain. In regime II, sweeping the angle in the basal plane back and forth produces a strong hysteresis of the Hall resistivity. In regime III, both  $E_x$  and  $E_y$  show sinusoidal variation and no hysteresis, indicating the spin texture of the system can be rotated easily as the magnetic field. The slight variation detected in  $\rho_H$  puts an upper limit on a possible in-plane anisotropy of  $\rho_H$ .

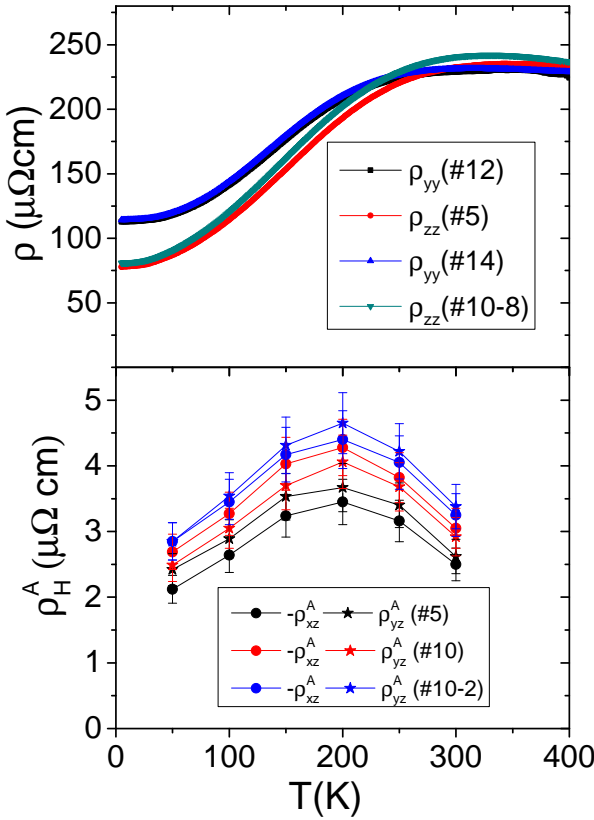


Figure S 5. a) Temperature dependence of the  $\rho_{yy}$  and  $\rho_{zz}$  in various samples. Both  $\rho_{yy}$  and  $\rho_{zz}$  measured in two different samples respectively shows almost identical behavior. b). The anomalous Hall resistivity on various samples at several temperatures. Combining the data in a), we deduced the Hall conductivity of Fig.2 in the main text.

## V. ANOMALOUS HALL EFFECT ON DIFFERENT SAMPLES

We have measured several samples to check the repeatability of our results, which are summarized in table I for 300 K and II for 50 K. Restrictions caused by samples dimensions are the reason some measurements were not performed. As seen in the table, the magnitude of  $\sigma_{yz}^A(B \parallel x)$  and  $\sigma_{xz}^A(B \parallel y)$  were very close. Fig. S5 shows the temperature dependence of resistivity and anomalous Hall resistivity in various samples. Fig. S6 displays the temperature of anomalous Hall conductivity data for fields along the  $x$  and  $y$  axes compared to previous reports [5, 6].

## VI. THE EXTRACTION OF $B_s$

We fitted the data between 0 to -200 mT for a positive to negative fields and 0 to 200 mT for negative to positive fields with an equation  $\rho_{ij} = \rho_0(1 - 0.5e^{-B_s/B})$  to extract

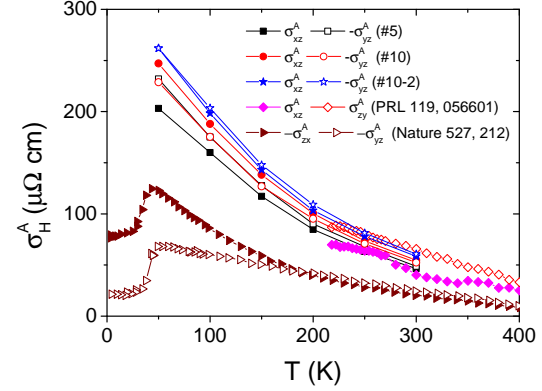


Figure S 6. a) The temperature-dependence of anomalous Hall conductivity in different samples and in previous reports.

Samples	$l_x$	$l_y$	$l_z$	$-\rho_{xz}$	$\rho_{yz}$	$\rho_{xx,yy}$	$\rho_{zz}$	$\sigma_{xz}$	$-\sigma_{yz}$	$-\frac{\sigma_{xz}}{\sigma_{yz}}$
	mm	mm	mm	$\mu\Omega\text{cm}$	$\mu\Omega\text{cm}$	$\mu\Omega\text{cm}$	$\mu\Omega\text{cm}$	S/cm	S/cm	
#5	0.5	0.6	2	2.5	2.62		232.5	46.5	48.7	0.955
#6	0.42	0.38	1.7		2.99				53.7	
#10	2.05	2.5	1.75	3.05	2.92			54.8	52.5	1.044
#10-2	2.05	1.15	1.75	3.25	3.38			58.4	60.7	0.962
#10-8	0.5	0.2	1.75				240.6			
#12	0.22	1.31	0.53			229.0				
#14	0.6	2.5	0.14			231.2				
Average				2.93	2.98	230.1	236.55	53.23	53.9	0.987

Table S I. Anisotropy of anomalous Hall effect in different samples at 300 K.

$B_s^+$  and  $B_s^-$  respectively.  $B_s$  is the average of  $B_s^+$  and  $B_s^-$ . The fig. S7 shows the procedure of the extraction of  $B_s$  in sample # 13-2 at 300 K.  $B_s$  for other samples were obtained by repeating this procedure.

## VII. COMPARISON WITH MNSI

The prototype spiral helimagnet MnSi has a non-trivial magnetic texture: a skyrmion lattice in its so-called A phase. Table III compares the physical properties of  $\text{Mn}_3\text{Sn}$  and MnSi.  $S_H^A$  is defined as  $\sigma_H^A/M$ . For MnSi, a

Samples	$l_x$	$l_y$	$l_z$	$-\rho_{xz}$	$\rho_{yz}$	$\rho_{xx,yy}$	$\rho_{zz}$	$\sigma_{xz}$	$-\sigma_{yz}$	$-\frac{\sigma_{xz}}{\sigma_{yz}}$
	mm	mm	mm	$\mu\Omega\text{cm}$	$\mu\Omega\text{cm}$	$\mu\Omega\text{cm}$	$\mu\Omega\text{cm}$	S/cm	S/cm	
#5	0.5	0.6	2	2.12	2.42		87.1	203.2	231.9	0.876
#6	0.42	0.38	1.7		2.95				271.0	
#10	2.05	2.5	1.75	2.69	2.49			247.1	228.8	1.08
#10-2	2.05	1.15	1.75	2.85	2.85			261.8	261.8	1
#10-8	0.5	0.2	1.75				90.8			
#12	0.22	1.31	0.53			118.2				
#14	0.6	2.5	0.14			119.8				
Average				2.55	2.68	119	88.95	237.4	248.4	0.985

Table S II. Anisotropy of anomalous Hall effect in different samples at 50 K.

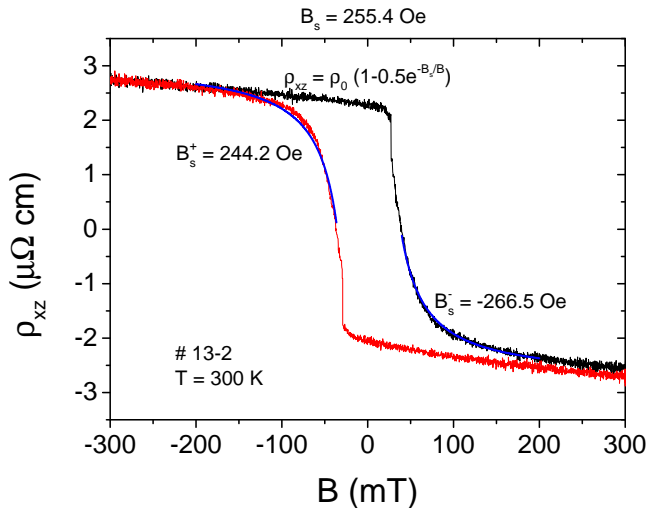


Figure S 7. An example of extraction of  $B_s$  in the sample # 13-2 at 300 K

	$\sigma_H^A$ S/cm	$\sigma_H^{THE}$ S/cm	M A/cm	$S_H$ V <sup>-1</sup>	$\frac{\sigma_H^{THE}}{\sigma_H^A}$
MnSi	56[7]	1.8[7]	293.8 [8]	0.19	0.032
Mn <sub>3</sub> Sn	232	113.7	10.75	21.6	0.49

Table S III. Comparison of magnetization and AHE in Mn<sub>3</sub>Sn (at 50K) with MnSi (at 28 K).

large AHE emerges below its Curie temperature and is almost proportional to its magnetization across a wide temperature window. The amplitude of the AHE of Mn<sub>3</sub>Sn is comparable to it at room temperature and 3 times larger at 100 K . While the magnetization of MnSi is 50 times larger than that of Mn<sub>3</sub>Sn. So the  $S_H^A$  are two to three orders higher than that in MnSi. The magnitude of  $S_H$  (the ratio of AHC to magnetization[8]) is exceptionally large in the former as highlighted previously[5]. Remarkably, a large fraction of the AHC in Mn<sub>3</sub>Sn is caused by real-space Berry curvature. As seen in the table, this is in sharp contrast with MnSi.

## VIII. THEORETICAL IN-PLANE ANISOTROPY

The calculated total energy of Mn<sub>3</sub>Sn as a function of the uniform spin angle rotation is shown in Fig. S8, which gives an indication about the in-plane single-ion anisotropy. One can see that the variation with angle is less than the convergence criteria 0.045 meV/Mn used in the calculations. This result is in agreement with the experimental finding according to which the spins can rotate very easily with rotating magnetic field. The band structure was also calculated for three different spin orientations (Fig. S9). No visible difference can be seen.

---

[1] J. P. Perdew, K. Burke, and M. Ernzerhof, Phys. Rev. Lett. **77**, 3865 (1996).  
[2] <http://elk.sourceforge.net>  
[3] S. Tomiyoshi, J. Phys. Soc. Jpn. **51**, 803 (1982).  
[4] P. Brown, V. Nunez, F. Tasset, J. Forsyth, and P. Radhakrishna, J. Phys. Condens. Matter **2**, 9409 (1990).  
[5] S. Nakatsuji, N. Kiyohara, and T. Higo, Nature **527**, 212 (2015).  
[6] Xiaokang Li, et al., Phys. Rev. Lett. **119**, 056601(2017).  
[7] A. Neubauer, C. Pfleiderer, B. Binz, A. Rosch, R. Ritz, P. G. Niklowitz, and P. Boöni. Topological Hall Effect in the A Phase of MnSi. Phys. Rev. Lett. **102**, 186602 (2009).  
[8] M. Lee, Y. Onose, Y. Tokura and N. P. Ong. Hidden constant in the anomalous Hall effect of high-purity magnet MnSi Phys. Rev. B **75**, 172403 (2007).

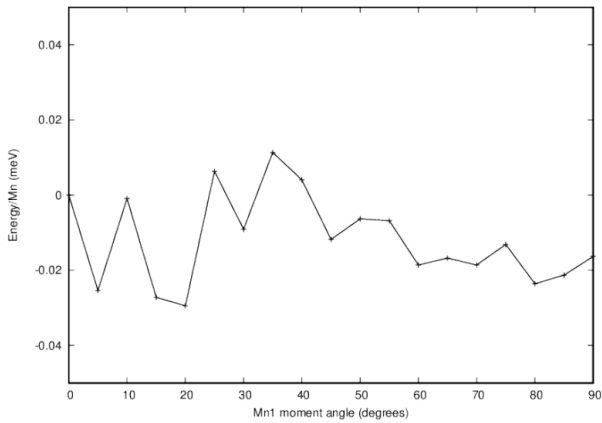


Figure S 8. The angle dependence of single-ion anisotropy

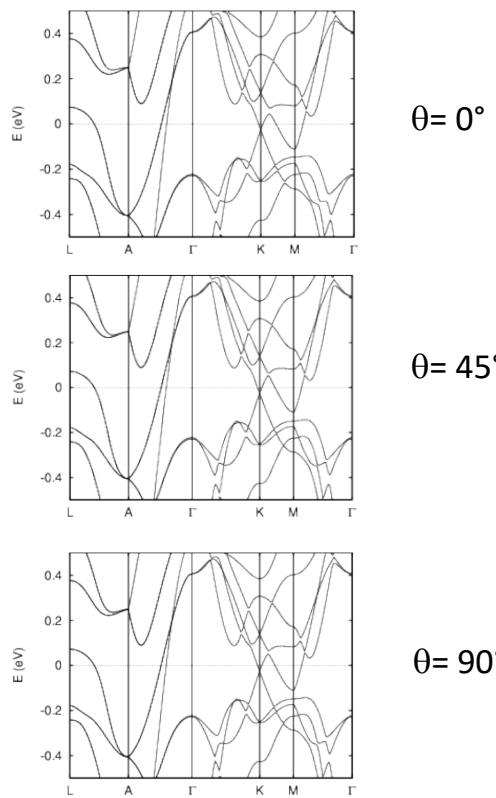


Figure S 9. Band structure for three different spin orientations.